

A large number of luminous infrared galaxies in the massive cluster Cl 0024+1654 [★]

D. Coia¹, B. McBreen¹, L. Metcalfe^{2,3}, A. Biviano⁴, B. Altieri², Y. Mellier^{5,6}, S. Ott⁷, J.-P. Kneib^{8,9}, and B. O'Halloran^{1,10}

¹ Department of Experimental Physics, University College, Belfield, Dublin 4, Ireland.

² XMM-Newton Science Operations Centre, European Space Agency, Villafranca del Castillo, P.O. Box 50727, 28080 Madrid, Spain.

³ ISO Data Centre, European Space Agency, Villafranca del Castillo, P.O. Box 50727, 28080 Madrid, Spain.

⁴ INAF/Osservatorio Astronomico di Trieste, via G.B. Tiepolo 11, 34131, Trieste, Italy.

⁵ Institut d'Astrophysique de Paris, 98 bis boulevard Arago, 75014 Paris, France.

⁶ Observatoire de Paris, 61 avenue de l'Observatoire, 75014 Paris, France.

⁷ Science Operations and Data Systems Division of ESA, ESTEC, Keplerlaan 1, 2200 AG Noordwijk, The Netherlands.

⁸ Observatoire Midi-Pyrénées, 14 avenue Edouard Belin, 31400 Toulouse, France.

⁹ California Institute of Technology, Pasadena, CA 91125, USA

¹⁰ Dunsink Observatory, Castleknock, Dublin 15, Ireland.

Received <date> / Accepted <date>

Abstract. Observations of the core of the massive cluster Cl 0024+1654, at a redshift $z \sim 0.39$, were obtained with the Infrared Space Observatory using ISOCAM at $6.7 \mu\text{m}$ (hereafter $7 \mu\text{m}$) and $14.3 \mu\text{m}$ (hereafter $15 \mu\text{m}$). Forty seven sources were detected at $15 \mu\text{m}$ and nineteen of them are spectroscopically identified with cluster galaxies. The remaining sources consist of four stars, one quasar, four foreground galaxies, one background galaxy and 18 sources with unknown redshift.

The spectral energy distributions (SEDs) and star formation rates were obtained for cluster members. The median infrared luminosity of the nineteen cluster galaxies is $\sim 1.3 \times 10^{11} \text{ L}_\odot$, with thirteen falling in the category of Luminous Infrared Galaxies (LIRGs). The [O II] star formation rates obtained for 6 cluster galaxies are one to two orders of magnitudes lower than the infrared values, implying that most of the star formation is missed in the optical because it is enshrouded by dust in the starburst galaxy.

There are no statistically significant differences between the spatial, radial and velocity distributions of the general population of cluster galaxies and those detected at $15 \mu\text{m}$, in the region mapped by ISOCAM. The colour-magnitude diagramme is given for the galaxies within that map. Only 30% of the galaxies that satisfy the Butcher-Oemler requirement were detected at $15 \mu\text{m}$, to the limiting sensitivity recorded. The counterparts of about two-thirds of the $15 \mu\text{m}$ sources are blue, luminous, star-forming systems and the type of galaxy that is usually associated with the Butcher-Oemler effect. HST images of these galaxies reveal a disturbed morphology with a tendency for an absence of nearby companions. Surprisingly the counterparts of the remaining one third of the $15 \mu\text{m}$ sources lie on the main sequence of the colour-magnitude diagramme which implies that they are early type galaxies. However in HST images they all have nearby companions and appear to be involved in interactions and mergers. Dust obscuration may be the major cause of the $15 \mu\text{m}$ sources appearing on the cluster main sequence. Recent changes in the galaxy population of the cluster are detected in the mid-infrared because of the bursts of obscured star formation.

Finally, the mid-infrared results on Cl 0024+1654 are compared with those from other clusters observed with ISOCAM. The number of $15 \mu\text{m}$ sources in Cl 0024+1654 exceeds that in Abell 370 by a large factor even though the two clusters are very similar in optical richness and redshift. The $15 \mu\text{m}$ cluster sources in Cl 0024+1654 are more luminous than those in Abell 1689 by about an order of magnitude. The dispersion in the number of luminous infrared cluster members seems to be related to the dynamical status of the cluster.

Key words. Galaxies: clusters: general – Galaxies: clusters: individual (Cl 0024+1654) – Infrared: galaxies

1. Introduction

Send offprint requests to: D. Coia, e-mail: dcoia@bermuda.ucd.ie

* Based on observations with ISO, an ESA project with instruments funded by ESA Member States (especially the PI countries: France, Germany, the Netherlands and the United Kingdom) and with the participation of ISAS and NASA

Clusters of galaxies contain thousands of members within a region a few Mpc in diameter, and are the largest known gravitationally bound systems of galaxies, having masses up to 10^{15} M_\odot for the richest systems. In hierarchical models clus-

ters of galaxies grow by accreting less massive groups falling along filaments at a rate governed by the initial density fluctuation spectrum, the cosmological parameters and the nature and amount of dark matter. In the cluster environment, newly added galaxies are transformed from blue, active star forming systems, to red, passive ellipticals, undergoing a morphological evolution stronger than that of field galaxies at a similar redshift (Gavazzi & Jaffe 1987; Byrd & Valtoten 1990; Abraham et al. 1996). The cluster galaxy population is also characterized by a lower star formation rate (SFR) than field galaxies of similar physical size and redshift (Couch et al. 2001; Lewis et al. 2002).

Butcher and Oemler (1978) have shown that clusters of galaxies generally have a fraction f_B of blue galaxies¹ that increases with cluster redshift, ranging from a value near 0 at $z = 0$, to 20% at $z = 0.4$ and to 80% at $z = 0.9$, suggesting a strong evolution in clusters (Rakos & Schombert 1995). The galaxies responsible for the Butcher-Oemler effect (hereafter BO effect) are generally luminous, spirals, and emission-line systems, with disturbed morphologies. Many mechanisms have been proposed to explain the complicated processes that occur in clusters, including ram pressure stripping of gas (Gunn & Gott 1972), galaxy harassment (Moss & Whittle 1997), galaxy infall (Ellingson et al. 2001), cluster tidal forces (Byrd & Valtoten 1990; Fujita 1998) and interactions with other cluster galaxies (Icke 1985; Moss & Whittle 1997). The main processes responsible for the morphological and spectral evolution of cluster galaxies have yet to be determined. Ram pressure and tidal effects can quench the star formation activity gradually because they operate over a period longer than 1 Gyr (e.g. Ghigna et al. 1998; Ramirez & de Souza 1998). Galaxy-galaxy interactions, galaxy harassment and cluster mergers can enhance it and produce changes in galaxy properties over timescales of ~ 100 Myr (e.g. Lavery & Henry 1986; Moore et al. 1996). Recent changes in the properties of the galaxies should be detectable in the mid-infrared because of the burst of star formation.

The Cosmic Infrared Background (CIRB) is a record of the optical and UV stellar emission over cosmic time. The bulk of the CIRB has now been resolved by the Infrared Space Observatory (ISO, Kessler et al. 1996) into sources with the major contribution from starburst galaxies at $z \sim 0.8$ and in the same redshift range as the AGNs responsible for the bulk of the X-ray background (Elbaz et al. 2002; Elbaz & Cesarsky 2003; Metcalfe et al. 2003a). The number of 15 μm sources exceeds by a factor of ten what would be expected in the local Universe if the relevant galaxy populations had not evolved over the past 10 billion years. The new class of sources are called Luminous and Ultraluminous Infrared Galaxies (LIRGs and ULIRGS, Sanders & Mirabel 1996, Genzel & Cesarsky 2000), that radiate the bulk of their emission in the far-infrared, and seem to be almost always the result of galaxy-galaxy interactions. They make a very minor contribution to the local

¹ Blue galaxies are defined as brighter than $M_V = -19.26$ (with $H_0 = 70 \text{ km s}^{-1} \text{ Mpc}^{-1}$) with rest-frame B-V colours at least 0.2 magnitudes bluer than those of the E/S0 galaxy sequence at the same absolute magnitude (Butcher & Oemler 1984; Oemler et al. 1997).

universe but were far more numerous at $z \sim 0.8$. They seem to represent a common phase in the evolution of most galaxies that gave rise to the majority of present day stars.

Studies of the global SFR show a decline by a factor of 3–10 since the peak of the star formation at $z = 1$ –2 (Madau et al. 1996; Steidel et al. 1998). The downturn in the global SFR and of the population of LIRGs and ULIRGs may be caused by galaxies running out of material and buildup of large scale structure in the Universe that changed the environment of galaxies. A study of the impact of the environment on galaxies in clusters could help in understanding the decrease in the global SFR. The history of star formation in clusters of galaxies is uncertain because optical observations, especially at high redshift, are incomplete and mid-infrared observations are only in their infancy. Variations in cluster properties, such as the dynamical status and the degree of subclustering, complicate the recognition of any evolutionary trend with redshift. Furthermore, the star formation history of clusters and that of the surrounding field are tightly related via the infall of field galaxies.

ISO made it possible to perform a number of mid-infrared observations of massive clusters of galaxies (e.g. Pierre et al. 1996; Lémonon et al. 1998; Boselli et al. 1998; Altieri et al. 1999; Barvainis et al. 1999; Contursi et al. 2001; Metcalfe et al. 2001, 2003a; Biviano et al. 2003). In these surveys the majority of the sources at 7 μm are cluster galaxies and the rest are field sources (including lensed background sources and foreground galaxies) or stars. The greater part of the 15 μm sources for which spectroscopic redshifts are available are found to be background sources (Metcalfe et al. 2003a). However this is not true for all clusters. Fadda et al. (2000) and Duc et al. (2002) found a higher proportion of 15 μm cluster sources in the cluster Abell 1689 at $z = 0.18$. The SFRs inferred from optical line emission using [O II] are about one tenth of those calculated from the infrared luminosities. The luminous mid-infrared galaxies in Abell 1689 are mainly morphologically disturbed star-forming spirals (Fadda et al. 2000; Duc et al. 2002). All the mid-infrared sources in Abell 1689 are detected in H _{α} , indicating that the star forming processes are not completely hidden (Balogh et al. 2002).

In this work we analyse the mid-infrared properties of the galaxy cluster Cl 0024+1654. The paper is organized as follows: Sec. 2 contains a description of the cluster. Sec. 3 describes the infrared observations and outlines the data reduction, source extraction and calibration processes. Sec. 4 presents the results, the model spectral energy distributions (SEDs) and star formation rates for cluster galaxies. Sec. 5 describes the spatial, redshift and colour properties of cluster galaxies and contains a description of Hubble Space Telescope images of some galaxies detected by ISOCAM. Sec. 6 makes a comparison between Cl 0024+1654 and other clusters studied with ISO, including Abell 1689, Abell 370, Abell 2390 and Abell 2218. The conclusions are in Sec. 7. The Appendix contains additional comments on some of the ISOCAM sources.

We adopt $H_0 = 70 \text{ km s}^{-1} \text{ Mpc}^{-1}$, $\Omega_\Lambda = 0.7$ and $\Omega_m = 0.3$. With this cosmology, the distance to the cluster is $D = 2140 \text{ Mpc}$ and 1'' corresponds to 5.3 kpc at the cluster redshift.

Fig. 1. The $15 \mu\text{m}$ map (red contours) of Cl 0024+1654 overlaid on a Very Large Telescope image taken in the V band with the FORS2 instrument (ESO program identification: 65.O-0489(A)). Black numbers refer to redundantly detected $15 \mu\text{m}$ sources (Table 2). Red numbers refer to non-redundantly detected $15 \mu\text{m}$ sources (Table 3). Each set of sources is labelled in order of increasing Right Ascension. Sources ISO_Cl0024_20 and ISO_Cl0024_21 are not shown in the figure because they are outside the boundary, and have a star and a faint galaxy, respectively, as optical counterparts. Blue circles denote $15 \mu\text{m}$ sources that are spectroscopically confirmed cluster galaxies. Letters in blue ($\alpha \div \delta$) identify four gravitational lensed images of the background galaxy associated with the spectacular giant arcs in the cluster field. North is up and East is to the left. All axes are in arcseconds. The centre of the ISO map is at R.A. 00 26 35.5 and DEC. 17 09 44.8 (J2000).

2. The cluster

Cl 0024+1654 is a rich cluster of galaxies at redshift $z \sim 0.395$ (Humason & Sandage 1957; Gunn & Oke 1975; Smail et al. 1993). It has a spectacular system of gravitationally lensed arcs (Fig. 1) that were first observed by Koo (1988) and subsequently studied by Mellier et al. (1991), Kassiola et al. (1994), Wallington et al. (1995) and Smail et al. (1997). The main arc

is split into segments (Colley et al. 1996; Tyson et al. 1998) and is the lensed image of a background blue galaxy at redshift $z = 1.675$ (Broadhurst et al. 2000). Unlike other clusters of galaxies, such as Abell 2218 or Abell 2390 that have arc-like features, Cl 0024+1654 does not have a central dominant cD galaxy.

Cl 0024+1654 was one of the two clusters examined by Butcher & Oemler (1978) in their first published work on

galaxy colours. The fraction of blue galaxies in Cl 0024+1654 is $f_B = 0.16$ which is much larger than the values of $f_B = 0.04$ and $f_B = 0.03$ for the Virgo ($z = 0.003$) and Coma ($z = 0.02$) clusters, respectively (Butcher & Oemler 1984; Dressler et al. 1985; Schneider et al. 1986).

The determination of the spectral types of galaxies has been made for the cluster and the field (Czoske et al. 2002; Balogh et al. 2002). Using a wide field HST survey of Cl 0024+1654, Treu et al. (2003) found that the fraction of early-type galaxies (E+S0) is highest ($\sim 73\%$) in the cluster core, declines rapidly to about 50% at ~ 1 Mpc, and reaches the background value of $\sim 43\%$ at the periphery of the cluster (at a radius of ~ 5 Mpc).

The mass profile of the cluster has been inferred from gravitational lensing analyses, kinematical analyses of the redshift of the cluster galaxies, and X-ray observations. The low value of the X-ray luminosity implies a mass 2 to 3 times smaller than that predicted by lensing models (Soucail et al. 2000; Ota et al. 2003). There are also differences among the lensing models. Broadhurst et al. (2000) favour a cuspy NFW profile for the mass distribution of the cluster (Navarro et al. 1997). Tyson et al. (1998) argue that this result requires an average cluster velocity distribution much higher than the measured value of $\sigma_v \sim 1150 \text{ km s}^{-1}$ (Dressler et al. 1999) and favour a uniform-density core for the halo mass profile. The weak lensing analysis made by Kneib et al. (2003), based on the extensive HST survey of Cl 0024+1654 (Treu et al. 2003), indicates that the region within 5 Mpc from the centre of the cluster is well fit by a steep NFW-like profile, and the isothermal fit is strongly rejected. Ota et al. (2003) analysed the X-ray emission from the cluster and found that an isothermal model with a mean temperature of 4.4 keV is a good fit to the temperature distribution. They also estimated the mass of the cluster on the assumption that the intracluster medium is in hydrostatic equilibrium, and confirmed that the mass inferred by X-ray observations is smaller than the mass predicted by lensing models by a factor of about 3.

During an extensive spectroscopic survey of Cl 0024+1654, Czoske et al. (2001) detected a significant number of galaxies at a redshift slightly lower than that of the cluster (Fig. 2). This concentration (component B) is interpreted as a small, less massive cluster superimposed on the main cluster (component A) and lying at a mean redshift of $z = 0.381$. Numerical simulations indicate that the two clusters in Cl 0024+1654 are involved in a high-speed collision along the line-of-sight to the cluster (Czoske et al. 2002). The relative velocity of the two components, derived from the difference in redshift of the two main galaxy concentrations, is about 3000 km s^{-1} . The collision scenario is not unusual because 30-40% of galaxy clusters have substructures that are detected in optical, X-ray and radio observations. These substructures indicate that the hosting clusters are not fully dynamically relaxed and might be currently undergoing, or have recently undergone, mergers (e.g. Mercurio et al. 2003). The important results obtained by Czoske et al. (2001, 2002) may give a new insight into the BO effect in medium and high redshift clusters. The impact of the two clusters could have triggered star formation in cluster galaxies, especially those on the leading edge of the smaller cluster, thus generating

the large number of blue galaxies observed in Cl 0024+1654. The differences between the results from the methods used to determine the mass of Cl 0024+1654 are naturally explained by the cluster collision (Czoske et al. 2002).

Fig. 2. The redshift distribution of 283 cluster members from the large sample of Czoske et al. (2001, 2002) showing the bimodal distribution of galaxies in Cl 0024+1654. The black boxes show the distribution of nineteen $15 \mu\text{m}$ cluster sources.

3. Observations, data reduction and source detection

3.1. Observations

The core of the cluster Cl 0024+1654 was observed at $7 \mu\text{m}$ and $15 \mu\text{m}$ using the LW2 and LW3 filters of the camera ISOCAM (Cesarsky et al. 1996) on board ISO. The ISOCAM long wavelength (LW) detector consisted of a 32×32 SiGa array. The observations were made on June 9 and June 15, 1997, in raster mode, with an on-chip integration time of 5.04 seconds in the $3''$ per pixel field of view, and cover an area of approximately 38 squared arcminutes. A discussion of the relevant observing strategy for ISOCAM can be found in Metcalfe et al. (2003a). (With the exception that the Cl 0024+1654 rasters were not “micro-scanned”. I.e. the raster step sizes were multiples of the array pixel size, whereas Metcalfe et al. describe rasters with step sizes involving fractions of a pixel’s dimensions). For each pointing of the raster, 14 readouts were performed at $7 \mu\text{m}$ and 10 at $15 \mu\text{m}$. Fifty readouts were taken at the beginning of each raster to allow for detector stabilization. The parameters used for the observations are given in Table 1, which also lists the sensitivity reached after data processing at the 5σ level. The diameter of the point spread function (PSF) central maximum at the first Airy minimum is $0.84 \times \lambda(\mu\text{m})$ arcseconds. The FWHM is about half that amount and Okumura (1998) obtained values of $3.3''$ at $7 \mu\text{m}$ and $5''$ at $15 \mu\text{m}$ for the PSF FWHM in the $3''$ per pixel field-of-view. The data were reduced and, to take advantage of a slight deliberate offset between the two

Table 1. Observational parameters used. The observations were made with the ISOCAM LW2 (filter width: 5 - 8.5 μm) and LW3 (filter width: 12 - 18 μm) filters at their respective reference wavelengths of 6.7 μm and 14.3 μm . On-chip integration time was always 5.04 seconds and the 3" per-pixel-field-of-view was used. M and N are the number of steps along each dimension of the raster, while dm and dn are the increments for a raster step. The sensitivity in μJy is given at the 5σ level. The table also includes the total area covered and the number of readouts per raster step. The rasters were repeated k times. Tot. t is the total time dedicated to each filter observation.

Filter	λ_{ref} (μm)	n Steps	dm (")	dn (")	Reads per step	area ($'^2$)	Done k times	Sensitivity (μJy)	Tot. t (sec)	
LW2	6.7	6	6	45	45	14	28.6	1	400	3138
LW3	14.3	14	14	21	21	10	37.8	2	140	22615

15 μm maps, were rebinned so that the final map has a pixel size of 1" with potential for slightly improved spatial resolution. The maximum depth is reached toward the centre of the rasters, where the dwell time per position on the sky is greatest. As recorded in Table 1, two rasters were made at 15 μm and a single raster at 7 μm that had a larger step size and less observation time (by a factor of 7).

3.2. Data reduction

The data were reduced using the *ISOCAM Interactive Analysis System* or CIA (Delaney & Ott 2002; Ott et al. 1997) in conjunction with dedicated routines, following the method described in Metcalfe et al. (2003a). The two 15 μm raster maps were normalized to their respective redundancy maps² and merged into a single raster, thus increasing the sensitivity of the map to faint sources. The program SExtractor (Bertin & Arnouts 1996) was used to detect sources. SExtractor was run separately on the two rasters and tuned to reproduce the sources found by visual inspection in each map. The tool was adjusted to recover sources where pixel values exceed the background level by 2.1σ over ten adjacent pixels. The selection criterion for the redundantly detected 15 μm sources (listed in Table 2) is very conservative because it requires the source to be detected in both rasters, which results in the rejection of faint sources that can be detected only in the merged map.

We therefore include an additional list of sources detected by SExtractor in the merged map (Table 3). The sources listed in italics in Table 3 were not recovered in the catalog automatically produced by SExtractor from the merged map. They are sources with significant mid-infrared fluxes (relative to locally measured noise in the map), all of which have an optical counterpart in the VLT map. The fluxes of these additional sources were computed manually by applying aperture photometry over a circular aperture centred on the infrared source, and having a diameter of 9". All the sources listed in Table 3 will be referred to as non-redundantly detected sources.

Since there was only one raster at 7 μm , an independent comparison of source detections was not possible and real

² The “redundancy” of a point in a raster map refers to the number of raster steps for which that point on the sky has been seen by some detector pixel. The term “redundantly detected source” used throughout this paper refers to a source detected in both of the 15 μm raster maps performed.

sources were considered to be only those having a 15 μm counterpart.

3.3. Montecarlo simulations and calibration

Montecarlo simulations were performed to calibrate the complex data reduction process by characterizing how it affects model sources with known properties inserted into the raw data, and to characterize the precision with which source signals could be recovered from the data. The procedure adopted is fully described in Metcalfe et al. (2003a). The simulations were performed independently for all rasters, and SExtractor was applied to the maps using the same parameters adopted for the photometry performed in the absence of fake sources. The recovered fluxes for the fake sources were typically 60-70% of the inserted model flux. The fluxes of the real sources were scaled according to the calibration factor determined from the simulations (Metcalfe et al. 2003a). Fluxes were converted to mJy using the typical filter specific ISOCAM calibration factors i.e. 1 ADUgs \equiv 0.43 mJy for LW2 and 1 ADUgs \equiv 0.51 mJy for LW3 (Delaney & Ott 2002), weighted by appropriate scaling factors to correct for detector responsive transient effects, taking the approach described by Metcalfe et al. (2003a) and references therein.

4. Results

The merged 15 μm map (Fig. 1) is overlaid on a V-band image of the cluster taken with the Very Large Telescope (VLT).

The list of sources detected on both individual 15 μm maps (i.e. redundantly detected sources) is given in Table 2 and the list of non-redundantly detected sources is in Table 3. The name of the ISOCAM source is composed of the satellite acronym (ISO), the partial name of the cluster (Cl0024), and an identification number assigned to each source, starting at 1 for the lowest RA source and increasing with RA (e.g. ISO_Cl0024_01 is Source 01 in Table 2).

The 7 μm fluxes for the stars, and their [7 μm]/[15 μm] flux ratios, are given in Table 4. The labels of the 7 μm sources are taken to be the same as their 15 μm counterparts. The fourth star detected at 15 μm (ISO_Cl0024_01) is outside the boundary of the 7 μm raster. No other sources were detected above the 5σ limit of $\sim 400 \mu\text{Jy}$.

The column named “Precision” in Tables 2 and 3 is a measure of the repeatability of the photometric results in the fake source simulations. For each source brightness the pre-

Table 2. The redundantly detected 15 μ m sources. The columns are (from left to right): source identification number in order of increasing Right Ascension; source flux and precision before calibration (in ADUs); source flux and precision after calibration (in mJy); Right Ascension and Declination of the infrared source (J2000); redshift and name of optical counterpart, if known. The redshift of source ISO_Cl0024_02 was taken from Schmidt et al. (1986). All other redshifts are from Czoske et al. (2001). The names of the stars are from HEASARC.

Source ID ISO_Cl0024_LW3	Signal (ADU)	Precision (\pm ADU)	Flux (mJy)	Precision (\pm mJy)	R.A. (J2000)	DEC. (J2000)	z if known	Name of optical counterpart if known
01	0.976	0.073	1.065	0.079	00 26 24.5	+17 08 17.0	Star	TYC 1180-82-1
02	0.544	0.059	0.592	0.064	00 26 26.5	+17 09 38.0	0.959	PC 0023+1653
03	0.323	0.056	0.352	0.060	00 26 27.2	+17 09 10.7	Star	N3231320329
04	0.331	0.056	0.361	0.060	00 26 31.0	+17 09 43.8		
05	0.276	0.056	0.302	0.060	00 26 31.1	+17 10 28.4		
06	0.762	0.069	0.827	0.074	00 26 31.2	+17 10 14.6	0.4005	
07	0.347	0.056	0.378	0.060	00 26 31.7	+17 10 20.4	0.2132	
08	0.203	0.056	0.222	0.060	00 26 32.0	+17 10 02.5	0.400	
09	0.327	0.056	0.357	0.060	00 26 36.1	+17 11 38.9		
10	0.330	0.056	0.360	0.060	00 26 36.8	+17 07 43.4	Star	EO903-0219757
11	0.195	0.056	0.214	0.060	00 26 36.8	+17 10 24.4		
12	0.385	0.056	0.420	0.060	00 26 37.9	+17 11 32.4		
13	0.244	0.056	0.267	0.060	00 26 39.1	+17 08 02.9		
14	0.735	0.069	0.798	0.074	00 26 40.6	+17 09 27.7	0.1393	
15	0.329	0.056	0.359	0.060	00 26 40.8	+17 11 43.9		
16	0.237	0.056	0.259	0.060	00 26 41.5	+17 11 00.4	0.3924	
17	0.390	0.056	0.425	0.060	00 26 42.0	+17 09 51.9	0.3935	
18	0.275	0.056	0.300	0.060	00 26 42.9	+17 09 40.6		
19	0.452	0.059	0.493	0.064	00 26 43.4	+17 09 10.7	0.3932	
20	1.233	0.074	1.338	0.080	00 26 48.1	+17 08 11.0	Star	EO903-0219375
21	0.580	0.059	0.631	0.064	00 26 48.2	+17 09 14.7		

cision is the 1-sigma scatter found in the recovered fluxes of fake sources of similar brightness inserted into the raw data. It should be noted that the ratio signal/precision is not, however, the signal-to-noise ratio; nor is it the significance of a source detection. The precision value carries information about pixel-to-pixel noise fluctuations, and also about small variations in calibration across the field which arise due to residual effects of glitches and flux-induced responsive transients acting on the high infrared background signal in the data stream. The quoted precision is a measure of the relative calibration accuracy within the sample recorded. The absolute flux calibration is, in addition, affected by factors such as imperfections in the knowledge of the detector response and responsive transient correction, and differences between the spectral shapes of measured sources with respect to the canonical calibration source for ISOCAM, which has a stellar spectrum. Experience over many surveys suggests an absolute calibration accuracy of $\pm 15\%$ for ISOCAM faint-source photometry due to accumulated systematic effects. The measured colour ratios for the stars listed in Table 4 are consistent with this, and give some confidence in the absolute calibration at the $\pm 15\%$ level. The significance of an individual source detection must be determined through an examination of the pixel-to-pixel signal variations in the map local to the source. All of the sources listed in Tables 2 and 3 have significance values greater than 5 sigma.

The number of redundantly and non-redundantly detected 15 μ m sources is 21 and 26, respectively, yielding a total of 47 sources. A search was performed for counterparts of the ISOCAM sources at other wavelengths, using a search radius of

6'' in HEASARC³ and NASA/IPAC Extragalactic Database⁴. Of the 21 redundantly detected sources (Table 2), 12 are identified with catalogued sources. Of these twelve, four are stars, one is a quasar (PC 0023+1653), five are cluster members and two are foreground galaxies. As for the 26 non-redundantly detected sources (Table 3), one is identified with a galaxy at $z = 0.5558$, two with foreground galaxies and fourteen with cluster galaxies. There is a total of 18 sources with unknown redshift and all have optical counterparts (Fig. 1).

We infer that the majority of the unidentified sources are not in the cluster by using the Log N-Log S distribution for field sources (as reported by e.g. Rowan-Robinson et al. 1997; Taniguchi et al. 1997; Altieri et al. 1999; Elbaz et al. 2002; Serjeant et al. 2000; Oliver et al. 2000; Lari et al. 2001; Gruppioni et al. 2002; Metcalfe et al. 2003a). The expected number of 15 μ m sources lensed by the cluster is estimated to be about 40 ± 15 , down to a flux-density limit of 100μ Jy, based on the results of the log N - log S distribution of Metcalfe et al. (2003a), of which we can expect to detect only a fraction in the Cl 0024+1654 maps. It follows that the 18 sources with unknown redshift could all be background sources, and most of them are likely to be so.

³ <http://heasarc.gsfc.nasa.gov/db-perl/W3Browse/w3browse.pl>

⁴ The NASA/IPAC Extragalactic Database (NED) is operated by the Jet Propulsion Laboratory, California Institute of Technology, under contract with the National Aeronautics and Space Administration.

Table 3. The non-redundantly detected 15 μm sources. The meaning of the columns is the same as in Table 2. The coordinates in italics refer to the sources that are not present in the SExtractor catalog and were manually extracted using aperture photometry with an aperture diameter of 9'' centred on the optical counterpart of the ISOCAM source. The redshifts for cluster sources, and for source ISO_Cl0024_32, are taken from Czoske et al. (2001). The redshift for source ISO_Cl0024_31 is from Treu (private communication).

Source ID ISO_Cl0024_LW3	Signal (ADU)	Precision (\pm ADU)	Flux (mJy)	Precision (\pm mJy)	R.A. (J2000)	DEC. (J2000)	z if known
22	0.282	0.056	0.308	0.060	00 26 24.3	+17 09 26.7	0.3937
23	0.210	0.056	0.230	0.060	00 26 30.9	+17 09 00.9	0.3935
24	0.279	0.056	0.305	0.060	00 26 30.9	+17 10 02.3	0.2150
25	0.221	0.056	0.242	0.060	00 26 31.2	+17 09 36.4	
26	0.249	0.056	0.272	0.060	00 26 31.1	+17 10 02.3	0.2150
27	0.210	0.056	0.230	0.060	00 26 31.6	+17 09 16.7	0.3998
28	0.181	0.056	0.199	0.060	00 26 32.6	+17 09 05.5	
29	0.154	0.056	0.169	0.060	00 26 32.7	+17 10 25.0	0.3965
30	0.156	0.056	0.172	0.060	00 26 33.6	+17 09 23.3	0.3902
31	0.263	0.056	0.287	0.060	00 26 34.9	+17 09 39.5	0.3979
32	0.200	0.056	0.219	0.060	00 26 35.7	+17 09 58.1	0.5558
33	0.206	0.056	0.226	0.060	00 26 35.6	+17 09 43.1	0.3871
34	0.158	0.056	0.174	0.060	00 26 36.1	+17 10 35.4	0.386
35	0.254	0.056	0.277	0.060	00 26 36.3	+17 10 20.5	
36	0.145	0.056	0.160	0.060	00 26 37.6	+17 09 28.1	0.390
37	0.230	0.056	0.252	0.060	00 26 38.9	+17 10 01.3	0.3953
38	0.208	0.056	0.228	0.060	00 26 40.6	+17 09 12.2	0.401
39	0.256	0.056	0.280	0.060	00 26 40.9	+17 09 53.0	0.3962
40	0.299	0.056	0.326	0.060	00 26 43.1	+17 08 30.7	
41	0.226	0.056	0.248	0.060	00 26 43.1	+17 10 44.6	
42	0.128	0.056	0.141	0.060	00 26 43.0	+17 08 50.3	0.3954
43	0.416	0.059	0.453	0.064	00 26 43.3	+17 08 24.1	
44	0.201	0.056	0.220	0.060	00 26 44.4	+17 09 38.6	
45	0.175	0.056	0.192	0.060	00 26 45.0	+17 09 03.0	
46	0.307	0.056	0.335	0.060	00 26 45.5	+17 07 40.5	0.3968
47	0.329	0.056	0.359	0.060	00 26 45.7	+17 08 29.8	

Table 4. The list of 7 μm sources with source flux exceeding 5σ of the local noise, and having 15 μm counterparts. From left to right: 15 μm source identification number as listed in Table 2; signal and precision of flux in ADU; flux and precision in mJy; Right Ascension, Declination; nature of the source; and finally the [7 μm]/[15 μm] colour ratio.

Source ID	Signal (ADU)	Precision (\pm ADU)	Flux (mJy)	Precision (\pm mJy)	R.A. (J2000)	DEC. (J2000)	Notes	[7 μm]/[15 μm]
03	1.461	0.084	1.685	0.098	00 26 27.0	+17 09 08.2	Star	4.8
10	1.276	0.081	1.468	0.095	00 26 36.5	+17 07 41.0	Star	4.1
20	3.806	0.129	4.427	0.151	00 26 47.9	+17 08 11.1	Star	3.3

4.1. Spectral Energy Distributions

Spectral energy distributions were computed for the cluster galaxies using the 15 μm fluxes in Tables 2 and 3, and a 5 sigma upper limit of 400 μJy for the 7 μm fluxes. The spectral range of the ISOCAM sources was extended by including measurements in the optical photometric bands and the near-infrared. The values were retrieved from the NASA/IPAC Extragalactic Database. The references to extensive observations of the sources are given in Table 5. The SEDs were modelled using the program GRASIL (Silva et al. 1998) and a redshift of $z = 0.395$ was adopted for all sources. Once the redshift is fixed, there are two free parameters to choose in the fit: one is the model SED, the other is the flux normalization for the SED model. The models that were considered are:

E: elliptical galaxy, with a star formation history characterized by an initial burst of star formation lasting 0.2-0.3 Gyr, and then a rapid decrease of the SFR, which is close to 0 at 1 Gyr;

Sa: early-type spiral, with a star formation history characterized by a SFR reaching a maximum after 1-2 Gyr, and then gently declining

Sc: late-type spiral, with a star formation history characterized by a gentle rise of the SFR, reaching a maximum at 10 Gyr, and then gently declining

M82: M82-like moderate starburst, observed 0.0 Gyr after the starburst began

Table 5. References to ISOCAM sources in existing archives. The first column lists the source number from Tables 2 and 3. The key to the references in Cols. 2 to 8 is Dressler & Gunn (1992, DG), Czoske et al. (2001, CKS), Schneider et al. (1986, SDG), Smail et al. (1997, SDC), McLean & Teplitz (1996, MT), Butcher & Oemler (1978, BO), Soucail et al. (2000, S) and Pickles & van der Kruit (1991, P). The table does not include the four stars or the quasar PC 0023+1653.

id	DG	CKS	SDG	SDC	MT	BO	Others
05	278				64		
06	264	267	113		22	34	S01
07	257	282			6		
08	237	289					
13	12						
14	47	444		797	4		
16	119	453					
17	43	459	146	834			
18	23			883			
19	3	474		928			
22	316	190					
23	198	262	223		123		
24	253			122			
26	249			92			
27	195	280		50			
29	246	304		55			
30	178	318	194	127	36	96	P85
33	148	374	161	343	7	65	P86
34	381						
36	101	412	186	573	11	87	P61
37	107	429		663	45		
38	29	446		813	56		
39	66	448		778	63		
42	471						
46	496						

Arp220: Arp220-like strong starburst, observed 0.5 Gyr after the starburst began.

While, formally, ages above 9-10 Gyr are not allowed at the cluster redshift, we also consider SED models older than this, since the model age is more an indication of the star formation history of the galaxy than its real age. The results of the SED fits are plotted in Fig. 3 and summarized in Table 6. In total, the best-fit SED models include 10 Sa, 5 Sc, 1 M82 and 2 E-type galaxies. For source ISO_Cl0024_34 the results were inconclusive because of a lack of optical data. Almost all sources are fit by SEDs which imply a high star formation rate. Moderate or strong starbursts are found in almost half of the sample.

4.2. Infrared and optical star formation rates for cluster members

The mid-infrared emission, free from dust extinction, is a reliable tracer of star formation (Genzel & Cesarsky 2000). The infrared emission from a galaxy is the sum of various contributions including:

- 1) continuum emission from dust particles
- 2) line emission from carriers of Unidentified Infrared Bands (UIBs)

- 3) line emission from ionized interstellar gas
- 4) emission from the evolved stellar population that dominates early-type galaxies
- 5) non-thermal emission from radio sources

The infrared spectrum of a galaxy depends on its morphological type and evolutionary status. For elliptical galaxies, the spectrum is similar to a blackbody continuum at a temperature of 4000-6000 K with a $[15\mu\text{m}]/[7\mu\text{m}]$ flux ratio of about 4.5, while for spiral galaxies the ratio of the $[15\mu\text{m}]/[7\mu\text{m}]$ flux is around 1 (Boselli et al. 1998). Starburst galaxies are characterized by a rapid increase in emission towards $15\mu\text{m}$ because of the contribution from very small grains, which are dust particles with radii of $\sim 10\text{ nm}$ that are abundant in star forming regions (Laurent et al. 2000).

The monochromatic luminosities at $15\mu\text{m}$, in units of solar luminosities, were obtained using the relationship (Boselli et al. 1998):

$$L_{15\mu\text{m}} = 4\pi D^2 F_{15\mu\text{m}} \delta_{15\mu\text{m}} \quad (1)$$

where $F_{15\mu\text{m}}$ is the flux at $15\mu\text{m}$ in mJy and $\delta_{15\mu\text{m}} = 5.04 \times 10^{12}$ Hz is the bandwidth of the LW3 filter. The total infrared luminosity was obtained from Elbaz et al. (2002):

$$L_{\text{IR}} = 11.1_{-3.7}^{+5.5} \times (\nu L_{\nu}[15\mu\text{m}])^{0.998} \quad (2)$$

The total infrared emission was also obtained directly from the best-fit SED model and provides an alternative determination of the total infrared luminosity. The total IR luminosities obtained from the two methods were compared and found to agree to within 30%. We adopt the IR luminosities obtained from Equation 2 for the cluster galaxies. The luminosities are listed in Table 6 and include the k-corrections obtained from the best-fit SEDs. The distribution of the total infrared luminosities for cluster galaxies is given in Fig. 4. The mid-infrared cluster members have total luminosities between $6.5 \times 10^{10} L_{\odot}$ and $4.1 \times 10^{11} L_{\odot}$, with a median value of $1.3 \times 10^{11} L_{\odot}$. Thirteen of the 18 galaxies have total infrared luminosities above $10^{11} L_{\odot}$, which classifies them as luminous infrared galaxies (LIRGs, $10^{11} L_{\odot} \leq L \leq 10^{12} L_{\odot}$, e.g. Genzel & Cesarsky 2000). The star formation rates, in units of solar masses per year, ρ , were derived using their dependence on L_{IR} (Kennicutt 1998):

$$\rho \simeq 1.71 \times 10^{-10} (L_{\text{IR}}/L_{\odot}) \quad (3)$$

The SFRs are listed in Table 6 and their distribution is displayed in Fig. 5. The infrared SFRs range between $\sim 11 M_{\odot} \text{ yr}^{-1}$ and $\sim 69 M_{\odot} \text{ yr}^{-1}$, with a median (mean) value of $22 (25) M_{\odot} \text{ yr}^{-1}$.

The $[\text{O II}]$ line is often used to determine the SFR in galaxies at intermediate redshift, when the Balmer hydrogen lines are outside the spectral range (e.g. Barbaro & Poggianti 1997; Jansen et al. 2000). There are several problems associated with this line. $[\text{O II}]$ is subject to dust extinction, and its strength depends heavily on the metallicity and ionization of the interstellar medium (Kennicutt 1998; Jansen et al. 2000). Furthermore, Balmer lines are more correlated to UV emission from young stars than $[\text{O II}]$. Therefore, the uncertainties in SFR computed from $[\text{O II}]$ are quite large. Nevertheless, the $[\text{O II}]$ line can be used to trace the SFR when better indicators are not available.



Fig. 3. SEDs for cluster members in Cl 0024+1654 detected at 15 μm . The horizontal axis is the wavelength in the cluster rest frame and the vertical axis is the flux normalized to the SED model. The data points are given by black dots and the model fit to the SED by a continuous line.

Table 6. Infrared luminosities and star formation rates for known cluster members in Cl 0024+1654. The columns list: LW3 identification number; luminosity at 15 μm using the transformation from Boselli et al. (1998); total infrared luminosity including the k-corrections using the best-fit SED and computed using the transformation from Elbaz et al. (2002); SFR from total IR luminosity using Kennicutt's (1998) transformation; EW[O II] line from Czoske et al. (2001) when available; SFR computed from the [O II] emission line using transformations from Kennicutt (1998); the ratio of the infrared SFR from Col. 4 to [O II] SFR and finally the best-fit SED model and age in Gyr.

id	$L_{15\mu\text{m}}$ (L_\odot)	L_{IR} (L_\odot)	SFR[IR] ($M_\odot \text{yr}^{-1}$)	EW[O II] (Å)	SFR[O II] ($M_\odot \text{yr}^{-1}$)	SFR[IR]/SFR[O II]	SED model (age)
6	8.66e+09	4.07e+11	69.2	-	-	-	Sc (14.0)
8	3.51e+09	1.65e+11	28.1	-	-	-	E (0.8)
16	2.56e+09	1.21e+11	20.5	-	-	-	Sa (3.0)
17	4.23e+09	1.99e+11	33.9	17.5	4.9	6.9	Sa (3.0)
19	5.91e+09	2.78e+11	47.2	-	-	-	M82 (13.0)
22	3.13e+09	1.47e+11	25.0	-	-	-	Sc (5.0)
23	2.73e+09	1.28e+11	21.8	-	-	-	E (0.4)
27	2.28e+09	1.07e+11	18.2	9.6	1.0	18.2	Sa (5.0)
29	1.66e+09	7.82e+10	13.3	-	-	-	Sa (7.0)
30	1.61e+09	7.59e+10	12.9	4.5	0.5	25.8	Sa (5.0)
31	2.96e+09	1.39e+11	23.7	-	-	-	Sc (15.0)
33	2.09e+09	9.85e+10	16.7	-	-	-	Sa (6.0)
36	1.50e+09	7.10e+10	12.1	-	-	-	Sa (10.0)
37	2.56e+09	1.20e+11	20.4	4.3	0.2	102.0	Sc (15.0)
38	2.28e+09	1.07e+11	18.3	-	-	-	Sa (4.0)
39	2.86e+09	1.34e+11	22.9	-	-	-	Sc (15.0)
42	1.38e+09	6.51e+10	11.1	5.0	0.8	13.9	Sa (8.0)
46	3.63e+09	1.71e+11	29.1	42.7	6.0	4.9	Sa (2.0)

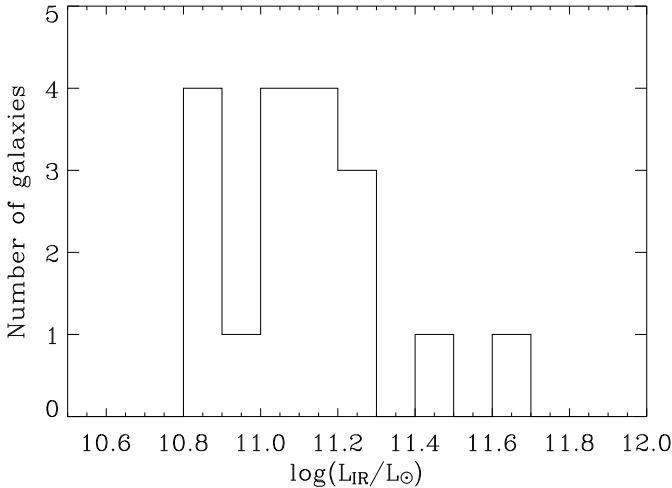


Fig. 4. The total infrared luminosity distribution for cluster members. The median value for L_{IR} is $1.3 \times 10^{11} L_{\odot}$.

The Equivalent Width (EW) of the [O II] line was available from Czoske et al. (2001) for only six of the mid-infrared cluster members. The [O II] line is redshifted into the V band and can be used to compute the optical SFR provided that the V-band magnitude is known. The monochromatic luminosity, L_V , was derived from the V-band magnitude in units of $\text{erg s}^{-1} \text{\AA}^{-1}$ using:

$$L_V = 4 \pi D^2 \times (3.08 \times 10^{22})^2 \times 10^{39-0.4m_V} \times 3.92 \times 10^{-5} \quad (4)$$

where D is the distance to the cluster in Mpc and m_V is the apparent magnitude in the V-band. The luminosity of the [O II] line is given by $L[\text{O II}] = \text{EW}[\text{O II}] \times L_V$ in units of erg s^{-1} . Finally, the SFR was obtained using $\rho \sim 1.4 \times 10^{-41} L[\text{O II}]$ in units of $M_{\odot} \text{ yr}^{-1}$. The SFRs derived from the EWs of the [O II] lines are listed in Table 6 and should be regarded as lower limits because no correction for extinction was applied. The median (mean) value of the optical SFR is 1 (2) $M_{\odot} \text{ yr}^{-1}$ and increases to ~ 3 (5) $M_{\odot} \text{ yr}^{-1}$ when the canonical value of 1 mag at H α (Kennicutt 1992), for extinction in the optical, is applied. The [O II] SFRs show a wide range, and are between one and two orders of magnitude lower than those obtained in the infrared. The ratios of $\text{SFR}[\text{IR}]/\text{SFR}[\text{O II}]$ range from 5 to 100 with a median value of 18 (Sec. 4.2). Therefore the vast majority of the star formation is missed when the [O II] line emission is used. A large fraction of the star formation in Cl 0024+1654 is enshrouded by dust. Duc et al. (2002) have arrived at a very similar conclusion for the cluster Abell 1689, which has many infrared sources.

In this sample, AGN activity does not seem to be a major contributor to the energy output of the systems. Only one of the mid-infrared sources (ISO_Cl0024_06) is a cluster X-ray source and is interpreted to be an AGN (C. Sanchez, private communication). Measurements of the H α and [N II] emission lines are required to further determine the AGN contribution to the mid-infrared emission (Balogh et al. 2002) and future radio observations could also help in determining the AGN contribution (Rengarajan et al. 1997; Dwarakanath & Owen 1999).

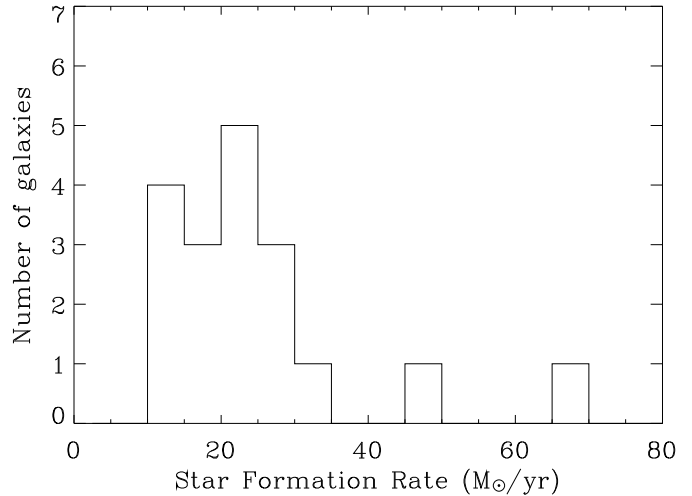


Fig. 5. The distribution of infrared SFRs for cluster galaxies. The median value is $\sim 22 M_{\odot} \text{ yr}^{-1}$.

5. Spatial, dynamical and colour properties of the 15 μm cluster galaxies

5.1. Spatial and velocity distributions

The spatial and radial distributions of the cluster galaxies, with and without detectable 15 μm emission, are given in Fig. 6. The isodensity contours and dots in Fig. 6(a) refer to galaxies belonging to component A, while the black boxes represent the cluster members with 15 μm emission. The latter are centrally condensed, corresponding to the high redundancy region of the raster map and to the peak of the redshift distribution of component-A galaxies. The Kolmogorov-Smirnov test reveals no statistically significant difference between the radial distributions of the galaxies with and without detectable 15 μm emission (Fig. 6(b)).

The redshift and velocity dispersion distributions for cluster galaxies with and without detectable 15 μm emission are given in Figs. 2 and 7. In particular, Fig 2 shows that the counterparts of 15 μm sources have redshifts near or beyond the redshift boundary between components A and B, and are members of the larger cluster. Two sources, ISO_Cl0024_33, with $z = 0.387$, and ISO_Cl0024_34, with $z = 0.386$, are close to the boundary. The velocity dispersion computed in the cluster rest-frame (Fig 7), using the biweight estimator (Beers et al. 1990) in the high redundancy region of the ISO map, is $\sigma_v = 914^{+59}_{-56} \text{ km s}^{-1}$ for a sample of galaxies of component A, while it is $\sigma_v = 1035^{+202}_{-170} \text{ km s}^{-1}$ for the 15 μm galaxies. The 15 μm sources have a flatter distribution than component-A galaxies (Fig. 2). The 15 μm source are associated mainly with spiral and emission-line galaxies, and studies of nearby clusters indicate a larger velocity distribution for this population (Biviano et al. 1997).

5.2. Colour-magnitude diagramme

The colour-magnitude diagramme for cluster galaxies is given in Fig. 8. It provides an important link between the optical and mid-infrared properties of the ISOCAM galaxies. Apparent

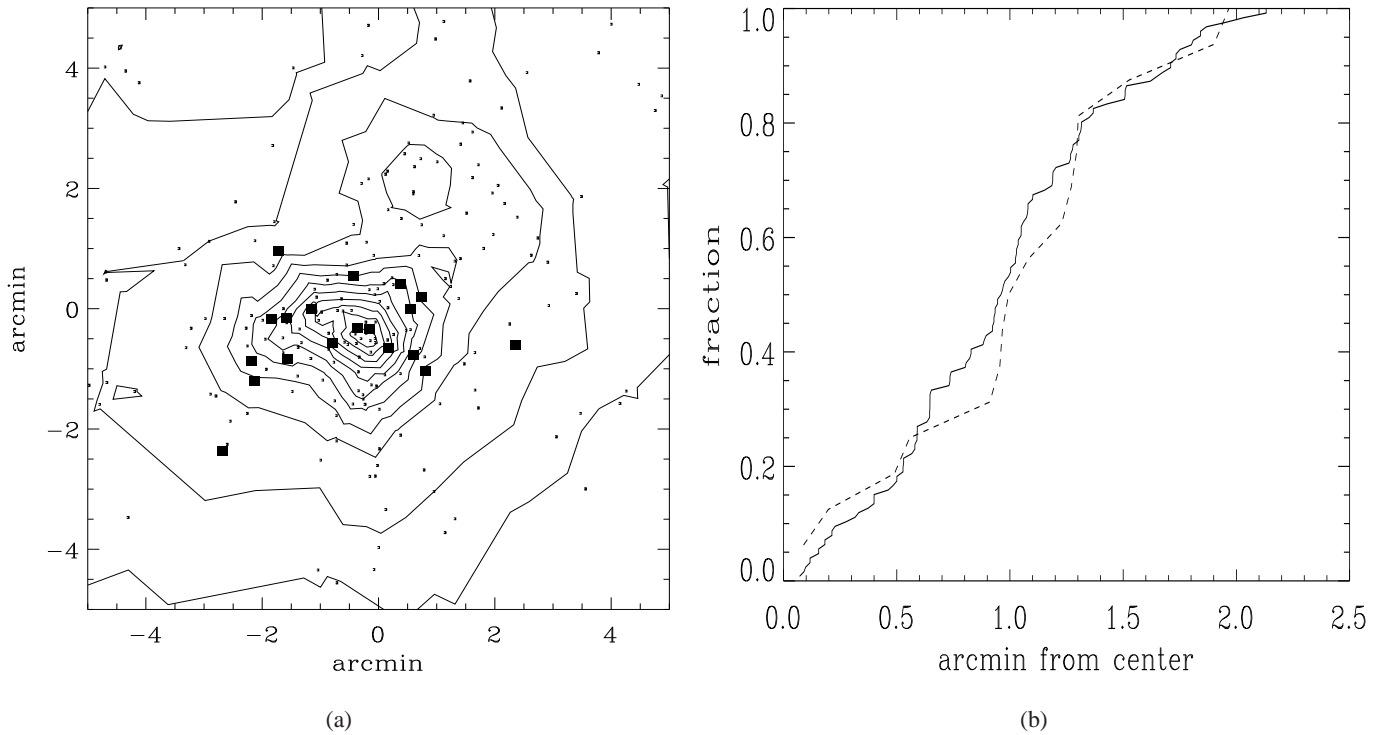


Fig. 6. (a) Adaptive Kernel map for cluster members. Black boxes represent the 15 μm sources while dots and isodensity contours trace the distribution of component-A galaxies. (b) Radial distribution from the centre of component-A galaxies (continuous line) and 15 μm cluster galaxies (dashed line) within the region covered by the ISOCAM observations.

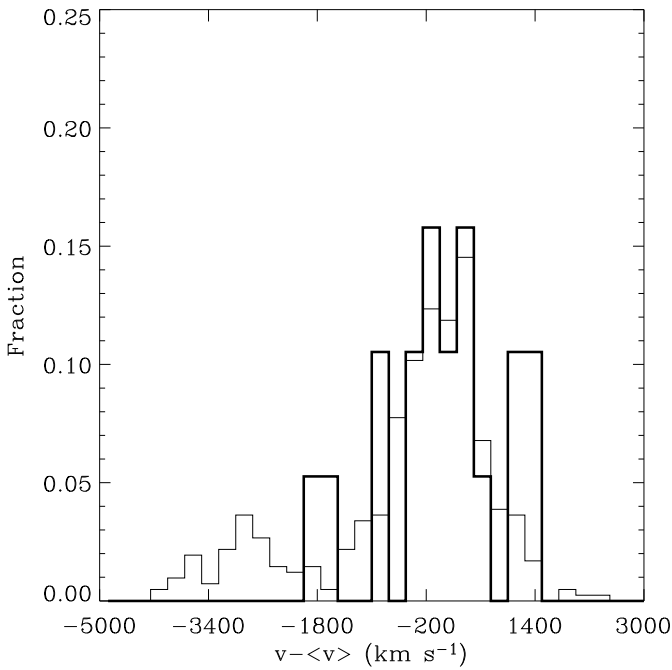


Fig. 7. The fractional distribution of velocities of 353 cluster galaxies belonging to component A (Czoske et al. 2001). The counterparts of the cluster members detected at 15 μm are displayed in bold. All velocities are in the cluster rest-frame.

magnitudes in the V and I bands are available from Czoske et al. (2001) for 17 of the 19 ISOCAM cluster galaxies. The cir-

cles represent component-A galaxies within the region mapped by ISOCAM. The spectroscopically confirmed mid-infrared cluster galaxies are indicated by filled circles and are labelled with the ISO source number. According to the definition given by Butcher & Oemler (1984), blue galaxies are those with an absolute magnitude, M_V , brighter than -19.26 (corrected for the adopted cosmology), and 0.2 mag below the cluster main sequence in the colour–magnitude diagramme. The cluster main sequence is at $V - I \sim 2$ (Fig. 8) and the reference M_V magnitude is transformed into the apparent I-band magnitude $m_I = 20.4$ when evolutionary effects and k-correction are taken into account. Section M of Fig. 8 contains the galaxies that satisfy the BO definition. Ten of the 15 μm galaxies fall in section M and satisfy the BO requirement. Only 30% of the cluster galaxies in section M are detected at 15 μm . However, this fraction increases to $\sim 40\%$ when galaxies brighter than $m_I = 19.8$ are considered. The non-detections are probably due to the lack of sensitivity of ISOCAM.

A HST image was available for part of Cl 0024+1654 from the MORPHS collaboration (Smail et al. 1997). This image is limited to the south-eastern region of the cluster core and contains thirteen of the 15 μm sources. For these galaxies, miniature maps centred on the ISOCAM source coordinates and having an area of $11 \times 11 \text{ arcsec}^2$ were obtained. Miniature maps were also obtained for an additional seven sources from HST archival images. The miniature maps are presented in Fig. 9.

HST images are available for 6 of the BO galaxies in section M of Fig. 8. ISO_Cl0024_17, ISO_Cl0024_38 and

Fig. 8. V - I colour-magnitude diagramme for component-A galaxies (empty circles) within the region mapped by ISOCAM. The seventeen 15 μm cluster galaxies (filled circles) are identified by their ISO source number from Tables 2 and 3. The V and I magnitudes were not available for the two sources ISO_Cl0024_31 and ISO_Cl0024_34. The galaxies in section M, which is enclosed by the dashed lines at $V - I = 1.8$ and $I = 20.4$, are BO galaxies. Surprisingly, seven of the 15 μm sources are in section N and not associated with BO galaxies.

ISO_Cl0024_39 do not have companions within a radius of 5''. However, the spiral structure of ISO_Cl0024_17 appears disturbed and ISO_Cl0024_39 has a box shape which may be the result of a past interaction or a merger. ISO_Cl0024_06 and ISO_Cl0024_46 have nearby galaxies with which they seem to be interacting. ISO_Cl0024_38 appears to be an undisturbed system. At least half of the galaxies in this small sample do not have nearby companions. The galaxies that appear currently isolated in the HST images might have been involved in interactions in the past. A relative velocity of 260 km s^{-1} or higher maintained for the last 100 Myr would have been sufficient for the interacting pair to move away from each other by at least 5'', i.e. out of the HST miniature map.

HST miniature maps for the five non BO galaxies in section N are also given in Fig. 9 and all have at least one nearby companion. ISO_Cl0024_33 and ISO_Cl0024_36 appear to be merging because they have multiple nuclei (ISO_Cl0024_33) and have at least two other companions. ISO_Cl0024_29, ISO_Cl0024_37 and ISO_Cl0024_42 show evidence of ongoing interactions (e.g. tidal bridges) with at least one nearby galaxy. Even though the number of infrared sources with HST maps is small, there seems to be a difference between the BO and non BO galaxies in the sense that the former tend not to have nearby companions whereas the latter do. The optical counterparts of the 15 μm sources are not passive early type galaxies as expected from their position on the main sequence of the colour-magnitude diagramme. This is a puzzling result because they should be elliptical or S0 galaxies and certainly not undergoing a major starburst. The counterparts however appear to be BO type galaxies that are involved in interactions and

mergers in the HST images. The SFRs obtained from the 15 μm measurements are essentially free from dust extinction and are much higher than the [O II] values (Table 6). The explanation for the difference in the SFRs is that there is significant obscuration in these dusty starburst galaxies. The same explanation could account for counterparts of some 15 μm sources lying on the cluster main sequence. We tested this possibility by plotting the dereddened SED of the 15 μm galaxies on the colour-magnitude diagramme. As expected the dereddened locations all shifted toward the BO region and in two cases (ISO_Cl0024_29 and ISO_Cl0024_37), out of six, the galaxies moved into the BO category (Fig. 8). Dust obscuration at least partially explains the unusual colours of the 15 μm sources on the cluster main sequence.

All 15 μm cluster sources have in common an excess of mid-infrared emission that sets them apart from the rest of the cluster members. In these systems, it is reasonable to conclude that the starburst is primarily triggered by interactions and mergers. Recent changes in the galaxy population reveal themselves in the mid-infrared and help identify the processes that cause the burst of obscured star formation. The infall of smaller groups into the cluster environment provides a way for promoting slow encounters and mergers within clusters (Mihos 2003). The slow encounters between galaxies are more able to drive instabilities than fast encounters.

The majority of the 15 μm cluster galaxies are LIRGs. Star forming episodes that are enshrouded by dust are commonly found in these galaxies in the field. The cause of the starburst phase of LIRGs in the local universe is still debated, but in the range of infrared luminosities measured with ISOCAM the

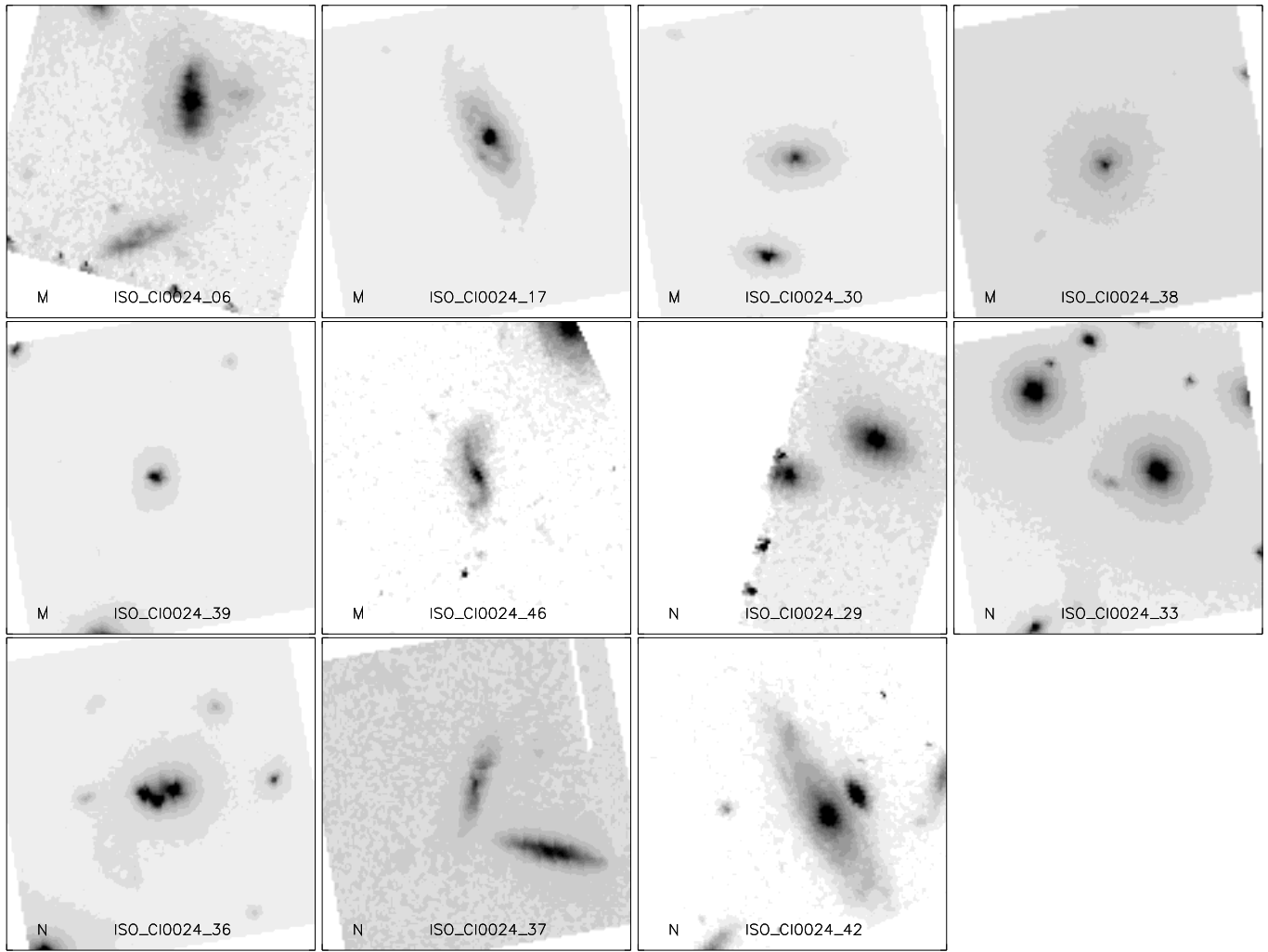


Fig. 9. Miniature maps obtained from HST images in the archive, and from the HST F814W image obtained by the MORPHS collaboration. The maps are centred on the $15 \mu\text{m}$ source coordinates and labelled with the source number in Tables 2 and 3. The letters M and N at the bottom left of the images give the positions of the cluster sources in the colour-magnitude diagramme (Fig. 8). All images are $11 \times 11 \text{ arcsec}^2$. North is up, East to the left.

starburst seems to be linked to mergers or interactions between pairs of spiral galaxies of unequal size and single galaxies in about one-quarter of the sources (Hwang et al. 1999; Ishida & Sanders 2001). The cause of the starburst in the $15 \mu\text{m}$ sources of Cl 0024+1654 seems to be consistent with what is observed in the local universe because of the evidence for interactions and mergers in the HST maps. Some examples of famous local LIRGs include Arp 244 (the Antennae, Vigroux et al. 1996), Markarian 297 (Metcalfe et al. 2003b) and the Wolf-Rayet galaxy NGC 1741 in the Hickson Compact Group 31 (O'Halloran et al. 2002). It is worth noting that none of the $15 \mu\text{m}$ cluster sources are ULIRGs. ULIRGs are a short lived phase in the interaction and merger of two spiral galaxies and hence their absence is not a major surprise.

6. Comparison of Cl 0024+1654 with other clusters observed by ISO

Observations of clusters of galaxies at high redshift ($z > 0.4$) with SCUBA have yielded an excess of sub-millimeter sources

with high values of the SFR (Best 2002). Here we compare the results of the observations of Cl 0024+1654 with those of four clusters of galaxies that were observed with ISOCAM at $15 \mu\text{m}$ (Fadda et al. 2000; Metcalfe et al. 2003a). The characteristics of the observations, and results for the five clusters, are summarized in Table 7. The observed areas and sensitivities are comparable for the first three clusters in Table 7, but somewhat smaller for Abell 2218, and much smaller for the ultra-deep observations of Abell 2390.

In comparing Cl 0024+1654 and Abell 370 it is important to note that they are at equivalent redshifts and were observed by ISOCAM with similar observational parameters, such as on-chip integration time, total areas observed in raster mode, and total observation times. The number of confirmed cluster sources in Cl 0024+1654 is 19 while the corresponding number in Abell 370 is 1 (Table 7). Abell 370 has a slightly lower redshift and higher sensitivity observations than Cl 0024+1654, and hence most of the $15 \mu\text{m}$ cluster sources in Cl 0024+1654 would have been detected in Abell 370, if present above 3σ . Even though the two clusters have reasonably similar values of

Table 7. Comparison between ISOCAM observations at 15 μm for different clusters. Data for Abell 370, Abell 2218 and Abell 2390 were taken from Metcalfe et al. (2003a), for Abell 1689 from Fadda et al. (2000) and Duc et al. (2002), for Cl 0024+1654 from this paper. From the first to the last column are listed: name and redshift of the cluster, total area scanned, sensitivity at 5 σ , flux of the weakest reported source in μJy , total observation time, total number of sources found including the number of sources without redshifts and stars, number of foreground sources, number of cluster sources, number of background sources, fraction of blue galaxies.

Cluster	z	Area (' ²)	Sensitivity (5 σ)	Faintest source (μJy)	Obs. t. (sec)	Tot. n. sources	Foreg. sources	Cluster sources	Backg. sources	f_B
Cl0024	0.39	37.8	140	141	22615	47	4	19	2	0.16 ± 0.02
A370	0.37	40.5	350	208	22688	20	3 [#]	1	15 [#]	0.21 ± 0.05
A1689	0.18	36.0	450	320	9500	18	1	12	4	0.18 ± 0.04
A2390	0.23	7.0	100	54	29300	28	0 [#]	4	24 [#]	0.14 ± 0.05
A2218	0.18	20.5	125	90	22000	46	0 [#]	7	37 [#]	0.11 ± 0.04

#: The numbers of foreground and background sources from Metcalfe et al. (2003a) are approximate, because they include a fraction of sources for which the cluster/non-cluster status was only inferred based on MIR colours.

f_B (cfr. Table 7), the number of luminous infrared galaxies is much larger in Cl 0024+1654 than in Abell 370. A population of luminous infrared galaxies is also absent from the central regions of the Virgo and Coma clusters.

A large number of cluster infrared sources was found in Abell 1689, which is at much lower redshift than Cl 0024+1654 and Abell 370. The total infrared luminosities for Abell 1689 galaxies range from $0.8 \times 10^{10} L_\odot$ to $6.2 \times 10^{10} L_\odot$, with a median value of $\sim 1.6 \times 10^{10} L_\odot$ (Duc et al. 2002), compared to the median value of $1.3 \times 10^{11} L_\odot$ for Cl 0024+1654. The 15 μm sources in Abell 1689 would not have been detected in the observations of Cl 0024+1654 and Abell 370 if they were present. The infrared SFRs in Abell 1689 are typically one to two orders of magnitude higher than obtained using the [O II] line luminosity. The average value of the ratio SFR[IR]/SFR[O II] is reasonably comparable for both clusters (it is ~ 11 for Abell 1689 and ~ 29 for Cl 0024+1654). Given the large uncertainties in the estimated SFR[O II], those ratios are not significantly different and imply similar dust extinction and observed star formation in both clusters. The colour-magnitude diagrams of the 15 μm sources in the two clusters are quite similar.

Abell 2390 and Abell 2218 are both rich clusters of galaxies at redshifts lower than Cl 0024+1654 but comparable to Abell 1689. The 15 μm observations of Abell 2390 and Abell 2218 are much more sensitive than those of Abell 1689, and in the case of Abell 2390 encompass a much smaller region (Table 7). The number density and luminosity of the 15 μm sources in Abell 2390 and Abell 2218 is much smaller than in Abell 1689.

It is interesting that the two clusters with the largest number of 15 μm sources, Cl 0024+1654 and Abell 1689, both show evidence for a recent collision or ongoing merger. Abell 1689 has a complex velocity structure that has substantial spread. In Abell 1689 there is evidence for three distinct groups that overlap spatially, but are well separated in velocity space (Girardi et al. 1997). The value of the blue fraction in Abell 1689 is controversial, with estimates ranging from 0.05 (Gudehus & Hegyi 1991) to 0.19 (Margoniner & de Carvalho 2001). The differences seem to be due to observational biases, uncertainties in the definition of the blue fraction, and background correction. The value of $f_B = 0.18$ in Table 7 is from Duc

et al. (2002). The number of luminous 15 μm sources can be, in part, explained by considering the dynamical status of Cl 0024+1654 and Abell 1689. Simulations made by Bekki (1999) show that the time-dependent tidal gravitational field existing in cluster-group mergers induces secondary starbursts by efficiently transferring large amounts of gas from the disk to the nucleus. The model establishes a link between the population of starburst or post-starburst galaxies and the presence of substructures in clusters. The existence of starburst galaxies in a merging cluster, and spread over a wide area, is an important prediction of this model which seems to be in agreement with the results from Cl 0024+1654 and Abell 1689.

In this context it is interesting to note that Dwarakanath & Owen (1999) found different radio source populations in two very similar clusters. The number density of radio sources in Abell 2125 ($z = 0.246$) exceeded that in Abell 2645 ($z = 0.25$) by almost an order of magnitude. The cluster Abell 2125, with the larger number of radio sources, also shows evidence for a merger.

7. Conclusions

The cluster Cl 0024+1654 was observed with ISO. A total of 47 sources were detected at 15 μm and all have optical counterparts. Sources with known redshift include four stars, one quasar, one background galaxy, four foreground galaxies and nineteen cluster galaxies. The remaining sources are likely to be background sources lensed by the cluster.

The spatial, radial and velocity distributions were obtained for the cluster galaxies and no statistically significant differences were found between the distributions of the 15 μm sources and other cluster galaxies in the region mapped by ISOCAM.

Spectral energy distributions were obtained for cluster members and used as indicators of both morphological type and star forming activity. Star formation rates were computed from the infrared and the optical data. The SFRs inferred from the infrared are one to two orders of magnitudes higher than those computed from the [O II] line emission, suggesting that most of the star forming activity is hidden by dust.

A colour-magnitude diagramme is given for cluster sources falling within the region mapped by ISOCAM. V and I-band magnitudes are available for 17 of the cluster sources, and 10 of these have colour properties that are consistent with Butcher-Oemler galaxies. HST images are available for 6 of these galaxies and they have disturbed morphologies with a tendency not to have nearby companions. The remaining seven 15 μm cluster galaxies have colours that are not compatible with Butcher-Oemler galaxies. HST images are available for five of these systems and all have nearby companion galaxies. These results suggest that interactions and mergers are responsible for the luminous infrared sources in the cluster.

The ISOCAM results obtained for Cl 0024+1654 are compared with observations of Abell 370, which is at a similar redshift, and also Abell 1689, Abell 2390 and Abell 2218. The number of 15 μm sources in Cl 0024+1654 exceeds that in Abell 370 by a large factor. The two clusters that have large numbers of mid-infrared sources, Cl 0024+1654 and Abell 1689, show evidence for past or ongoing collisions. The merging process seems to be responsible for the large dispersion in the number of 15 μm sources in clusters at similar redshift.

Acknowledgements. We thank Laura Silva for valuable discussions regarding the spectral energy distributions. D.C. gratefully acknowledges the hospitality of ESA's ISO Data Centre (IDC) at Vilspa, Spain, where part of this work was completed. JPK acknowledges support from CNRS as well as from Caltech.

The ISOCAM data presented in this paper was analysed using "CIA", a joint development by the ESA Astrophysics Division and the ISOCAM Consortium. The ISOCAM Consortium is led by the ISOCAM PI, C. Cesarsky. This research made use of the NASA/IPAC Extragalactic Database (NED) which is operated by the Jet Propulsion Laboratory, California Institute of Technology, under contract with the National Aeronautics and Space Administration.

Appendix A: Additional notes on some mid-infrared sources

A.1. Redundantly detected sources

ISO_Cl0024_02 Radio quiet quasar PC 0023+1653 (Schmidt et al. 1986) at a redshift of 0.959 with an X-ray luminosity $L_{\text{X}} = 1.4 \times 10^{44} \text{ erg s}^{-1}$ (Soucail et al. 2000).

ISO_Cl0024_04 The 15 μm map has two bright regions that may contain contributions from two optical counterparts. There are no measured redshifts.

ISO_Cl0024_05 The 15 μm emission appears to have contributions from various galaxies in the field-of-view. No redshifts are available for these sources although they seem to be in the cluster.

ISO_Cl0024_06 Most of the 15 μm emission is centred on a cluster galaxy at redshift $z = 0.4005$ (Table 2), the brightest of the two galaxies in Fig. 9. The model fit to the SED is an Sc (Fig. 3). The source was also detected in X-rays with ROSAT (Böhringer et al. 2000). The optical identification for the ROSAT source is uncertain because there are two sources in the error box. One of the sources is a typical cluster galaxy while the second is a star-forming foreground galaxy ($z = 0.2132$). The cluster galaxy is closer to the 15 μm coordinates and was adopted as the mid-infrared counterpart. It is the only cluster AGN detected so far in Cl 0024+1654.

ISO_Cl0024_12 The redshift of the optical counterpart on the VLT image is not known. The 15 μm emission is centred on one galaxy and partially extends to two very faint optical sources that are north of the main optical source.

ISO_Cl0024_13 The redshift of the optical counterpart on the VLT image has not been measured. The 15 μm emission is centred on the bright optical source and is partially elongated towards two other sources on the VLT map.

ISO_Cl0024_14 The optical counterpart is a large, edge-on, late type, foreground spiral galaxy at $z = 0.1393$. The 15 μm emission is centred on the galaxy and has contributions from several other sources. The HST image reveals a disturbance of the spiral structure. The EW for the H_{α} line is 3.6 \AA (Czoske et al. 2001).

ISO_Cl0024_17 The optical counterpart is a cluster galaxy with $z = 0.3935$. The HST image (Fig. 9) reveals a spiral galaxy with an inner ring, a smoother outer arm (Smail et al. 1997) and bright knots. The best fit to the SED is found for an Sa model (Fig. 3).

ISO_Cl0024_18 The redshift of the optical counterpart is not available. At the 15 μm coordinates, the HST image shows two interacting spiral galaxies and a tidal arm.

ISO_Cl0024_19 The 15 μm emission is concentrated on a cluster galaxy. An M82 model is the best fit to the SED (Fig. 3) while the HST image shows a highly inclined disk galaxy with a bright knot at the northern border of the galaxy.

ISO_Cl0024_21 The source is outside the boundaries of the VLT and HST images (Fig. 1) and has a faint optical counterpart (Fig. 4d in Czoske et al. 2001).

A.2. Non-redundantly detected sources

ISO_Cl0024_30 On the HST image there is a chain of at least four spiral galaxies with the southern galaxy interacting with a very faint source. The peak of the 15 μm emission is taken to be the first source on the northern end of the chain. With this assumption, the best-fit to the SED is found for an Sa galaxy. The equivalent widths of $[\text{O}\text{II}]$ and H_{δ} are $4.5 \pm 1 \text{ \AA}$ and $-2.1 \pm 1.1 \text{ \AA}$ respectively (Czoske et al. 2001).

ISO_Cl0024_31 The optical counterpart is in the core of the cluster and centred on one of the cluster galaxies. The mid-infrared emission is extended towards other galaxies of the central group.

ISO_Cl0024_32 The optical counterpart is a background spiral galaxy ($z = 0.5558$) with two bright knots in the HST image. The extended 15 μm emission has two lobes extending approximately North-South. The galaxy has EW $[\text{O}\text{II}] = 29.7 \pm 2.0 \text{ \AA}$ and EW $[\text{H}_{\delta}] = -3.1 \pm 0.7 \text{ \AA}$ (Czoske et al. 2001).

ISO_Cl0024_37 The HST image shows three nearby galaxies. The 15 μm emission is centred on the warped eastern galaxy. The galaxy is a cluster member and is best fit by an Sc model (Fig. 3).

ISO_Cl0024_38 The faint 15 μm source coincides with a cluster member that has a faint nucleus and a large disk, on the HST image. The best fit to the SED is an Sa model (Fig. 3).

ISO_Cl0024_42 The HST image shows two (interacting?) galaxies and a third galaxy with a tidal arm orientated towards the other two galaxies. The best fit to the SED of the main galaxy is an Sa model (Fig. 3).

References

Abraham, R. G., Smecker-Hane, T. A. Hutchings, J. B., et al., 1996, *ApJ*, 471, 694

Altieri, B., Metcalfe, L., Kneib, J.P, et al. 1999, *A&A*, 343, L65

Balogh, M. L., Couch, W. J., Smail, I., Bower, R. G., & Glazebrook, K. 2002, *MNRAS*, 335, 10

Barbaro, G. & Poggianti, B. M. 1997, *A&A*, 324, 490

Barvainis, R., Antonucci, R., & Helou, G. 1999, *AJ*, 118, 645

Beers, T. C., Flynn, K., & Gebhardt, K. 1990, *AJ*, 100, 32

Bekki, K. 1999, *ApJ*, 510, L15

Bertin, E. & Arnouts, S. 1996, *A&AS*, 117, 393

Best, P. N. 2002, *MNRAS*, 336, 1293

Biviano, A., Katgert, P., Mazure, A., et al. 1997, *A&A*, 321, 84

Biviano, A., Metcalfe, L., McBreen, B., et al. 2003, *Memorie della Societa Astronomica Italiana*, 74, 266

Böhringer, H., Soucail, G., Mellier, Y., Ikebe, Y., & Schuecker, P. 2000, *A&A*, 353, 124

Boselli, A., Lequeux, J., Sauvage, M., et al. 1998, *A&A*, 335, 53

Broadhurst, T., Huang, X., Frye, B., & Ellis, R. 2000, *ApJ*, 534, L15

Butcher, H. & Oemler, A. 1978, *ApJ*, 219, 18 (BO)

Butcher, H. & Oemler, A. 1984, *ApJ*, 285, 426

Byrd, G. & Valtonen, M. 1990, *ApJ*, 350, 89

Cesarsky, C. J., Abergel, A., Agnese, P., et al. 1996, *A&A*, 315, L32

Colley, W.N., Tyson, J.A., & Turner, E.L. 1996, *ApJ*, 461, L83

Contursi, A., Boselli, A., Gavazzi, G., Bertagna, E., Tuffs, R., & Lequeux, J. 2001, *A&A*, 365, 11

Couch, W. J., Balogh, M. L., Bower, R. G., et al. 2001, *ApJ*, 549, 820

Czoske, O., Kneib, J.-P., Soucail, G., Bridges, T., Mellier, Y., & Cuillandre, J.-C. 2001, *A&A*, 372, 391 (CKS)

Czoske, O., Moore, B., Kneib, J.P., & Soucail, G. 2002, *A&A*, 386, 31

Delaney, M. & Ott, S. 2002, "ISOCAM Interactive Analysis User's Manual", Version 5.1, SAI/96-5226/Dc

Dressler, A., Gunn, J. E., & Schneider, D. P. 1985, *ApJ*, 294, 70

Dressler, A. & Gunn, J. E. 1992, *ApJS*, 78, 1 (DG)

Dressler, A., Smail, I., Poggianti, B., et al. 1999, *ApJS*, 122, 51

Duc, P.A., Poggianti, B., Fadda, D., et al. 2002, *A&A*, 382, 60

Dwarakanath, K. S. & Owen, F. N. 1999, *AJ*, 118, 625

Elbaz, D., Cesarsky, C., Chanial, P., et al. 2002, *A&A*, 384, 848

Elbaz, D. & Cesarsky, C. J. 2003, *Science*, 300, 270

Ellingson, E., Lin, H., Yee, H. K. C., & Carlberg, R. G. 2001, *ApJ*, 547, 609

Fadda, D., Elbaz, D., Duc, P.-A., et al. 2000, *A&A*, 361, 827

Fujita, Y. 1998, *ApJ*, 509, 587

Gavazzi, G. & Jaffe, W. 1987, *A&A*, 186, L1

Genzel, R. & Cesarsky, C. J. 2000, *ARA&A*, 38, 761

Ghigna, S., Moore, B., Governato, F., et al. 1998, *MNRAS*, 300, 146

Girardi, M., Fadda, D., Escalera, E., et al. 1997, *ApJ*, 490, 56

Gruppioni, C., Lari, C., Pozzi, F., et al. 2002, *MNRAS*, 335, 831

Gudehus, D. H. & Hegyi, D. J. 1991, *AJ*, 101, 18

Gunn, J. E. & Gott, J.R. 1972, *ApJ*, 176, 1

Gunn, J. E. & Oke, J. B. 1975, *ApJ*, 195, 255

Humason, M. L. & Sandage, A. R. 1957 in *Carnegie YearBook* 1956 (Carnegie Institute of Washington), p.61

Hwang, C., Lo, K. Y., Gao, Y., Gruendl, R. A., & Lu, N. Y. 1999, *ApJ*, 511, L17

Icke, V. 1985, *A&A*, 144, 115

Ishida, C. M. & Sanders, D. B. 2001, *AAS*, 198, 34.16

Jansen, R. A., Fabricant, D., Franx, M., & Caldwell, N. 2000, *ApJS*, 126, 331

Kassiola, A., Kovner, I., Fort, B., & Mellier, Y. 1994, *ApJL*, 429, L9

Kennicutt, R. C. 1992, *ApJ*, 388, 310

Kennicutt, R. C. 1998, *ARA&A*, 36, 189

Kessler, M., Steinz, J., Anderegg, M., et al. 1996, *A&A*, 315, L27

Kneib, J.-P., Hudelot, P., Ellis, R.S., et al. 2003, submitted to *ApJ* (astro-ph/0307299)

Koo, D. 1988, in *Large-Scale Motions in the Universe*, Rubin, V.G., Cayne, G.V. (eds), Princeton Univ. Press, p. 513

Lari, C., Pozzi, F., Gruppioni, C., et al. 2001, *MNRAS*, 325, 1173

Laurent, O., Mirabel, I., Charmandaris, V., et al. 2000, *A&A*, 359, 887

Lavery, R. J. & Henry, J. P. 1986, *ApJ*, 304, L5

Lémonon, L., Pierre, M., Cesarsky, C. J., et al. 1998, *A&A*, 334, L21

Lewis, I., Balogh, M., De Propris, R., et al. 2002, *MNRAS*, 334, 673

Madau, P., Ferguson, H. C., Dickinson, M. E., et al. 1996, *MNRAS*, 283, 1388

Margoniner, V. E., de Carvalho, R. R., Gal, R. R., & Djorgovski, S. G. 2001, *ApJ*, 548, L143

McLean, I. S. & Teplitz, H. 1996, *AJ*, 112, 2500 (MT)

Mellier, Y., Fort, B., Soucail, G., Mathez, G., & Cailloux, M. 1991, *ApJ*, 380, 334

Mercurio, A., Girardi, M., Boschin, W., Merluzzi, P., & Busarello, G. 2003, *A&A*, 397, 431

Metcalfe, L., McBreen, B., Kneib, J.P., & Altieri, B. 2001, *IAU Symposium*, 204, 217

Metcalfe, L., Kneib, J.P., McBreen, B., et al. 2003a, *A&A*, 407, 791

Metcalfe, L., O'Halloran, B., McBreen, B., et al. 2003b, in prep

Mihos, J. C. 2003, *Carnegie Observatories Astrophysics Series*, Vol. 3, Cambridge: Cambridge Univ. Press, in press astro-ph/0305512

Moore, B., Katz, N., Lake, G., Dressler, A., & Oemler, A. 1996, *Nature*, 379, 613

Moss, C. & Whittle, M. 1997, *Revista Mexicana de Astronomia y Astrofisica Conference Series*, 6, 145

Navarro, J.F., Frenk, C.S., & White, S. 1997, *ApJ*, 490, 493

O'Halloran, B., Metcalfe, L., McBreen, B., et al. 2002, *ApJ*, 575, 747

Oemler, A.J., Dressler, A., & Butcher, H.R. 1997, *ApJ*, 474, 561

Okumura, K. 1998, *ESA ISOCAM PSF report*, http://iso.vilspa.esa.es/users/expl_lib/CAM/psf_report.ps.gz

Oliver, S., Rowan-Robinson, M., Alexander, D. M., et al. 2000, *MNRAS*, 316, 749

Ota, N., Hattori, M., Pointecouteau, E., & Mitsuda, K. 2003, submitted to *ApJ* (astro-ph/0306580)

Ott, S., Abergel, A., Altieri, B., et al. 1997, in *ASP Conf. Ser. Vol. 125, Astronomical Data Analysis Software and Systems (ADASS) VI*, ed. G. Hunt & H.E. Payne, eds., (San Francisco: ASP), 34

Pickles, A. J. & van der Kruit, P. C. 1991, *A&AS*, 91, 1 (P)

Pierre, M., Aussel, H., Altieri, B., et al. 1996, *A&A*, 315, L297

Rakos, K. D. & Schombert, J. M. 1995, *ApJ*, 439, 47

Ramirez, A. C. & de Souza, R. E. 1998, *ApJ*, 496, 693

Rengarajan, T. N., Karnik, A. D., & Iyengar, K. V. K. 1997, *MNRAS*, 290, 1

Rowan-Robinson, M., Mann, R., Oliver, S., et al. 1997, *MNRAS*, 289, 490

Sanders, D. B. & Mirabel, I. F. 1996, *ARA&A*, 34, 749

Schmidt, M., Schneider, D.P., & Gunn, J.E. 1986, *ApJ*, 306, 411

Schneider, D., Dressler, A., & Gunn, J. 1986, *AJ*, 92, 523 (SDG)

Serjeant, S., Oliver, S., Rowan-Robinson, M., et al. 2000, *MNRAS*, 316, 768

Silva, L., Granato, G. L., Bressan, A., & Danese, L. 1998, *ApJ*, 509, 103

Smail, I., Ellis, R. S., Aragon-Salamanca, A., et al. 1993, *MNRAS*, 263, 628

Smail, I., Dressler, A., Couch, W. J., et al. 1997, *ApJS*, 110, 213 (SDC)
Soucail, G., Ota, N., Böhringer, H., et al. 2000, *A&A*, 355, 433 (S)
Steidel, C. C., Adelberger, K. L., Giavalisco, M., Dickinson, M., &
Pettini, M. 1999, *ApJ*, 519, 1
Taniguchi, Y., Cowie, L. L., Sato, Y., et al. 1997, *A&A*, 328, L9
Treu, T., Ellis, R. S., Kneib, J., et al. 2003, *ApJ* (in press) astro-
ph/0303267
Tyson, J. A., Kochanski, G. P., & dell'Antonio, I. P. 1998, *ApJ*, 498,
L107
Vigroux, L., Mirabel, F., Altieri, B., et al. 1996, *A&A*, 315, L93
Wallington, S., Kochanek, C., & Koo, D.C. 1995, *ApJ*, 441, 58

This figure "figure_1.jpg" is available in "jpg" format from:

<http://arxiv.org/ps/astro-ph/0310317v1>

This figure "figure_2.jpg" is available in "jpg" format from:

<http://arxiv.org/ps/astro-ph/0310317v1>

This figure "figure_3.jpg" is available in "jpg" format from:

<http://arxiv.org/ps/astro-ph/0310317v1>

This figure "figure_8.jpg" is available in "jpg" format from:

<http://arxiv.org/ps/astro-ph/0310317v1>